Chemistry Africa (2023) 6:945–966
https://doi.org/10.1007/s42250-022-00544-9

ORIGINAL ARTICLE

Synthesis, Spectroscopic, DFT Study, and Molecular Modeling of Thiophene-Carbonitrile Against Enoyl-ACP Reductase Receptor

Tabe N. Ntui[1] · **Emmanuella E. Oyo-Ita**[2] · **John A. Agwupuye**[3] · **Innocent Benjamin**[4] · **Ishegbe J. Eko**[5] · **Emmanuel I. Ubana**[3] · **Kokolo M. Etiowo**[1] · **Emereze C. Eluwa**[1] · **Anna Imojara**[4]

Received: 28 August 2022 / Accepted: 14 November 2022 / Published online: 10 December 2022

Abstract

The studied compound was synthesized by the reaction of diazotized 4-Aminobenzene and 2-amino-4-(4-aminophenyl) thiophene-3-carbonitrile (AATC). The synthesized structure was experimentally characterized using FT-IR and GC–MS followed by detailed computational investigations of the experimental structure and a subsequent application for molecular docking against the InhA receptors. The density functional theory (DFT) and time-dependent DFT calculations were performed using the B3LYP/6–311++G(d,p) method. The experimental vibrational frequencies were compared with the theoretical vibrational wavenumbers and the entire vibrational assignments were made solely to characterize the potential energy distributions (PED) using the Veda04 programme. The Fukui functions, MEP, and ADCH analysis were used to describe the reactive sites of the studied structure. Conceptual density functional theory (CDFT) and Frontier molecular orbitals (FMO) were used to characterize the reactivity parameters of the whole molecule while the aromaticity index was used to identify the most aromatic fragment of the studied compound. Natural bond orbital (NBO) analysis aided in describing the interactions that lead to the highest stabilization of the molecule and the interactions that undergo Intra- and Intermolecular charge transfer. Nonlinear optical property (NLOP) of APTC was also studied in order to ascertain its importance in technology such as optoelectronic devices. The Molecular docking studies were used to study the inhibitory action of the studied structure against some InhA proteins [an NADH-dependent enoyl-acyl carrier protein reductase (enoyl-ACP reductase)] using Auto-Dock vina software. The absorption, distribution, metabolism, excretion, and toxicity (ADMET) analysis was carried out using pq SCM to compare the drug physicochemical properties with standard drug isoniazid.

Keywords Azo dye · Synthesis · Spectroscopy · DFT · ADMET · Docking

1 Introduction

Organic molecules known as azo compounds have an azo group –N=N– linked to their molecular structure. They are extensively employed in the production of dyes, printing, cosmetics, and medicine application [1]. The manufacture of azo dye has increased in recent years, and its importance is still felt. Over 60% of all dyes are made up of it, and it is frequently utilized [2, 3]. They are well-known for their therapeutic uses, such as antiseptics, antioxidants, antidiabetic, antineoplastic, analgesic, anti-inflammatory, antiviral and tubercular, and antitumor activities [4, 5], in addition to their colors, which are determined by the presence of azo groups bound to aromatic heterocycles, benzene rings, and naphthalenes. They are distinguished by the covalent bond that forms between their chemical groups and the textile substrate. The simplest methods for creating azo compounds

✉ Innocent Benjamin
benjamininnocent53@gmail.com

[1] Department of Chemistry, Faculty of Physical Sciences, Cross River University of Technology, Calabar, Nigeria

[2] Department of Biochemistry, Faculty of Physical Sciences, Cross River University of Technology, Calabar, Nigeria

[3] Department of Pure and Applied Chemistry, Faculty of Physical Sciences, University of Calabar, Calabar, Nigeria

[4] Department of Microbiology, Faculty of Biological Sciences, University of Calabar, Calabar, Nigeria

[5] Polymer and Textile Engineering, Ahmadu Bello University, Zaria, Kaduna, Nigeria

are diazotization and coupling [2]. As a result, tuberculosis (TB) remains the most lethal infectious disease in the world, as it is an airborne, fatal infection caused by the Mycobacterium tuberculosis bacterium despite several approaches that have been employed to curtail the dreaded disease. More so, it is a bacterial infection that is the second leading cause of death. Although there is TB therapy available, it has killed 1.5 million people and afflicted 10 million people in 2019. Whilst MDR and XDR-TB should make TB eradication possible, DOTS has failed to do so, with more people dying each day. Furthermore, Patients with MDR and XDR-TB require extremely complex treatment. As a result, fresh anti-TB medication has been sought for by researchers. Also I t has been determined that bedaquiline is the first brand-new TB medication to be introduced in more than 40 years. Since Mycobacterium tuberculosis can be controlled while also causing fewer adverse effects, finding such medications is a significant problem for researchers. Herein, the studied dye was prepared using the aforementioned techniques, specifically diazotization and coupling of the primary amine with the intermediates 4-aryl-2-aminothiophene-3-carbonitrile. The synthetic substance, a monoazo dye, has a color spectrum that is primarily between orange and brown, a blue shift (negative solvatochromism), little wavelength absorption, and strong solvent polarity. As many azo polymers are highly photoresponsive and used in dye-sensitizing solar cells and electro-optical activities, light absorption and electronic excitation are distinguishing characteristics of the azo cores [6]. The synthesized azo molecule was subjected to an experimental and theoretical research in order to determine its complete vibrational frequencies, electron excitation analysis, reactivity, and inhibitory actions against InhA proteins. Additionally, a number of theoretical features including vibrational analysis, NBO, CDFT, density of states (DOS), FMO, Aromaticity index, MEP, and population analysis were researched. Utilizing the Lipinski RO5 rule and ADMET, the pKSCM web server model was utilized to determine the physical–chemical similarities between various drugs (absorption, distribution, metabolism, excretion, and toxicity).

A molecular docking simulation was conducted based on the promising outcome of the examined compound's drug-likeness. Because it investigates the impact or interaction between a potential drug (a ligand) and a protein, molecular docking is essential for drug discovery. In the current study, the authors looked at the examined structure's inhibitory effects on a few InhA crystallographic structures. The short chain dehydrogenase/reductase family includes the INHA gene, which codes for the InhA enzyme and is important in the production of fatty acids. Mycolic acid is produced in part by the fatty acid biosynthesis pathway enzyme InhA. This is due to its reliance on fatty acid synthase 2 and NADH trans enoyl-acyl ACP carrier protein (FASII). The long chain fatty acids known as mycolic acids make it feasible for the human pathogens Mycobacterium TB and Mycobacterium leprae to construct cell walls. The oldest and most well-recommended synthetic medication for the treatment of tuberculosis is isoniazid, a key target of InhA [7]. The modeled structure was docked with crystallographic structures of InhA in order to explore its antitubercular activity against the enzyme because azo compounds are well recognized to have therapeutic effects. The reduced molecule (ligand) was docked with the chosen InhA proteins with PDB entry codes 1P44, 1P45, 3FNE, and 4TZK [8, 9] in order to screen the chemical under investigation as a potential InhA inhibitor.

2 Experimental and Computational Methods

2.1 Experimental

2.1.1 Synthesis of 2-Amino-4-(4-Aminophenyl)-5-(Phenyldiazenyl)Thiophene-3-Carbonitrile (AATC)

After being cooled at 0 to 5 °C in an ice bath, a well-stirred solution of 1-aminobenzene (10.2 g, 0.05 mol) in 2 N HCl (15 ml) was diazotized with 1 N NaNO2 solution (3.5 g, 0.05 mol; in 20 ml water). Over the course of 30 min, the sodium nitrite was gradually added while stirring. For an additional two hours, the reaction mixture was agitated. Using starch iodide paper, which produced a blue color, the combination was then examined for full diazotization. When the mixture failed the test, more sodium nitrite was cautiously added drop by drop until the mixture produced a positive color that remained steady for a few minutes. To eliminate extra nitrous acid, some urea was also added. A well-stirred solution of the coupling component was added gradually to the aforementioned cold diazonium solution. Distilled water (25 ml) and hydrochloric acid (6 ml, 36%) were used to react a solution of diazotized 1-aminobenzene (14.8 g, 0.05 mol at 95% purity) with a solution of 2-amino-4-(4-aminophenyl)thiophene-3-carbonitrile (4.9 g, 0.05 mol) during the course of 30 min at 0–5 °C. The mixture was swirled for three hours while being kept at a temperature between 3.5 and 4 degrees Celsius. The acquired dye was filtered out, allowed to air dry, and then weighed. Figure 1 reports the synthesis route of the produced azo dye.

2.1.2 Spectral Measurements

Fourier transform infrared (FT-IR) measurements were made using an Agilent CARY 630 FTIR at room temperature in a KBr disc (thermal nicolet) in the wavenumber range

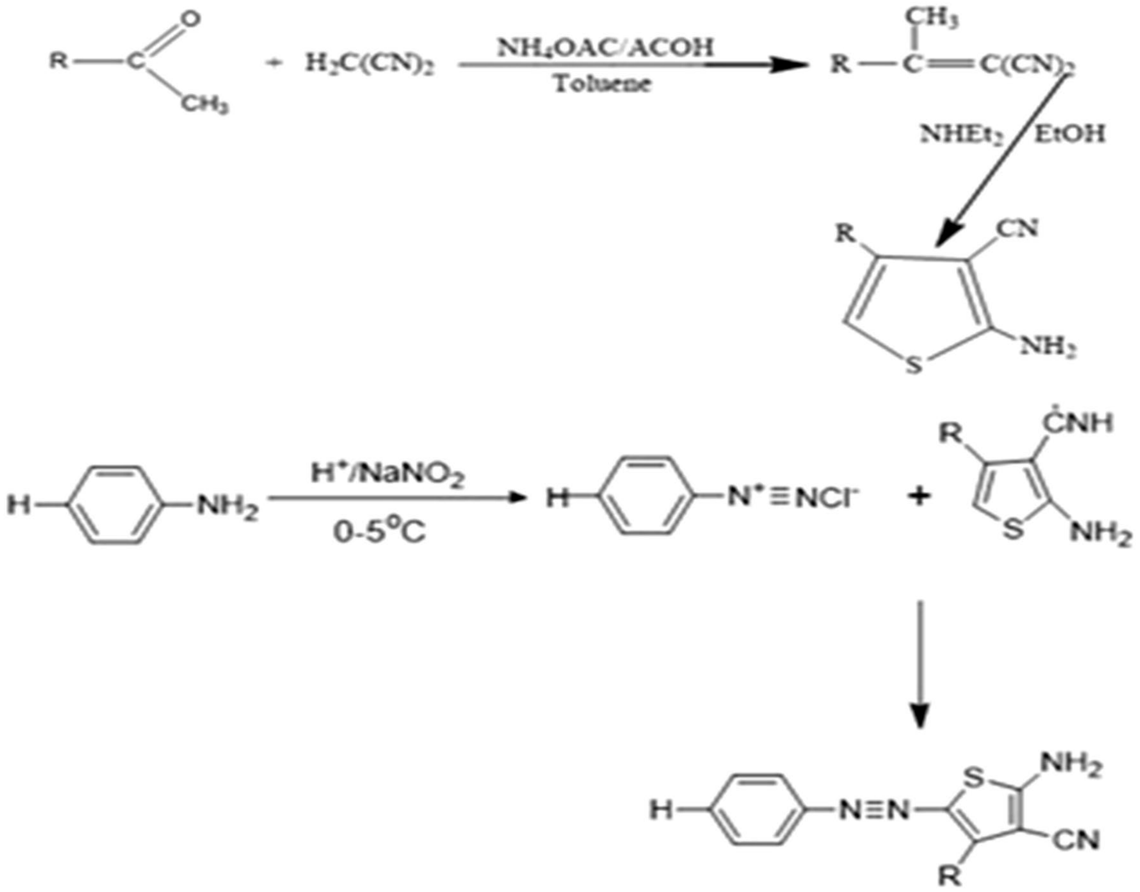

Fig. 1 Synthesis route of the studied azo compound

4000–450 cm ^(−1). The units of all absorption bands are cm ^(−1).

GCMS spectroscopy: Using the electron spray ionization (ESI) method, mass spectra were captured on Agilent Technologies 6400 mass spectrometers. The information reveals a peak at [M–Na]^+

2.2 Computational Details

2.2.1 Quantum Mechanical Calculations

Due to its efficiency, the Gaussian 09W computational software [10] was used to do the quantum chemical calculations of the simulated AATC in order to derive the molecular structure, along with hybrid-exchange correlation three-parameter functional level (B3LYP) and 6-311++G(d,p) basis set [11]. Using DFT (B3LYP)/6-311++G(d,p) functional, the optimal molecular geometry of AATC has been predicted in the gaseous phase. The Gaussian calculation setup was done using the GaussView application 6.0, which was also used to display the results [12]. The VEDA04 program [13] additionally with the help of the GaussView visualizer utilized the optimized molecular geometry for the computation of the vibrational frequencies and vibrational assignments of fundamental normal modes of vibration on the basis of PEDs. Utilizing the GaussView application, the population analysis was chosen in order to do NBO calculations. The time-dependent DFT (TD-DFT) method was used to obtain the hole-electron excitation energies, electronic transitions, and visual representations of the different excitation states. The results were used by the Multiwfn analyzer created by Tian-Lu [14] to obtain all the properties of excitation for the different excitation states in the studied compound. The GaussView program was used to visualize the structure's MESP. Conceptual Density Functional theory, DFT, was utilized to get aromaticity indices, ADCH population for charge analysis, and the output data was employed by Multiwfn analyzer to compute results.

2.2.2 Pharmacological Investigations

Using the Molinspiration web server [16], the molecular characteristics and Lipinski (Rule of Five) RO5 [15] for AATC and Isoniazid (standard medication) were calculated.

With a focus on the absorption, distribution, and toxicity characteristics, a comprehensive ADMET (absorption, distribution, metabolism, excretion, and toxicity) was generated for isoniazid (the reference medication) using the pKCSM online program [17].

2.2.3 Molecular Docking Details

AutoDock 4.2 software was used to analyze molecular docking [18]. From the Brook-haven Protein data repository, the crystallographic structures of InhA (or, in one case, *E. coli* FabI) in association with inhibitors were taken (PDB ID: 1P44, 1P45, 3FNE, 4TZK). Using Discovery studio, the co-crystallized ligand, water molecules, and co-factors were removed, preparing the protein for docking. The structure of the ligand was drawn in Avogadro and then converted to PDB format. The protein was converted to SDF format using the Swiss PDB reader, which also removed certain protein residues that were thought to not be a part of the protein. The Autodock Vina tools were located in Pyrex, where docking was done and findings were obtained. A cubic grid box of 40 A (X, Y, Z) with a spacing of 0.375 A was constructed utilizing Auto dock tools incorporated in Pyrex in order to choose active site to prevent blind docking [19, 20]. The reduced molecule (ligand) was embedded in the protein 1P44, (X = 109.4876, Y = 109.2504, Z = 109.0562), with an exhaustiveness of 8, and the grid map was produced in the active site. Additionally, the AATC was docked to protein 1P45, and a grid map with the coordinates (X = 85.8796, Y = 90.5921, Z = 76.8279) and an exhaustiveness of 8 was created. The resulting grid map for protein 3FNE has an exhaustiveness of 8 and has the coordinates (X = 104.2502, Y = 104.6975, Z = 104.4952). The grid map created by the APTC docking with protein 4TZK is (X = 69.34818, Y = 71.1787, Z = 70.6503), with an exhaustiveness of 8. All docked ligands' binding affinities were chosen with an RMSD value of 0. Because the better docking pose matches the ligand's binding mode on the protein, the binding affinity with RMSD value of 0 is chosen. The outcomes were examined using Pymol software [21] and PyRx in both two- and three-dimensional orientation. Then, in both 2D and 3D formats, the ligand–protein interactions were examined using Biovia Discovery studio software [22].

3 Results and Discussion

3.1 Vibrational Analysis

Finding the vibrational modes connected to pertinent and specific chemical structures of the computed substance in question is the aim of the vibrational analysis. A non-linear molecule with N atoms can have a maximum of (3N-6) normal modes of vibration as active fundamentals that can be observed [23]. The investigated compound consists of 36 atoms and 102 vibrational modes. 35 of the 102 vibrational modes are bending, 34 are stretching, and 33 are torsional. Due to a confluence of electron correlation effects and flaws in the DFT basis set, the DFT estimated vibration wavenumber are frequently many orders of magnitude larger than the empirically observed wave number. In order to accurately fit the results, scale factors are used to match the DFT estimated wave numbers with those of the observed ones. In order to lessen the overall deviance, a scale factor of less than one (0.96) was employed. The theoretical IR and potential energy distributions associated with the fundamental modes in terms of vibrational assignments are shown in Table 1 together with the results of the DFT-B3LYP/6-311++G(d,p) calculation. The supplementary information's Fig S1a, b shows the computed and experimental FT-IR. The absence of a few peaks with such low intensities can be confirmed by theoretically predicted FT-IR intensity values.

N–H Vibrations: The characteristic R-NH_2 vibrations for primary amines have been assigned in the region 3500–3200 cm^{-1} [23]. Bend in primary amines results in a broadband in the range 1640–1560 cm^{-1} [24]. The present calculations place the R-NH_2 stretching modes at 3451 and 3358 cm^{-1} in experimental FT-IR. The H–N–H band was also observed experimentally to occur at 1640 cm^{-1}. The bands at 3516 cm^{-1} and 3417 cm^{-1} for R-NH_2 stretch and 1628 cm^{-1} for N–H bond B3LYP/6-31++G(d,p) set are in good agreement with observed spectral data. These are intense stretching modes and identified from the PED in Table 1.

C–N Vibrations: C–N stretch occurs in the region 1350–1000 cm^{-1} [25, 26]. The aromatic C–N stretch was observed to occur at 1334 cm^{-1}. Theoretically, the computed wavelength of C–N stretch is observed at 1322 cm^{-1}.

–N=N– Vibrations: The N=N stretching vibrations for azo compounds occurs in the region 1500 cm^{-1} and 1400cm^{-1} [27]. The present calculations show that –N=N– vibrations occur at 1439 cm^{-1} while the computational frequency calculated at B3LYP/6-31++G(d,p) basis set was observed at 1403 cm^{-1}.

=C–H Vibrations: The aromatic ring shows the occurrence of C–H stretching vibration modes in the range 3300–3000 cm^{-1} region [28]. The title compound observe =C–H stretching vibrational mode at 3239 cm^{-1} for experimental FT-IR while the computational frequency of the title compound was observed at 3106 cm^{-1}. These are intense stretching modes and identified from the PED.

C–C and C=C Vibrations: The Aromatic C=C and C–C stretching vibrations (Aromatic ring stretching vibrations) occurs in the region 1625–1400 cm^{-1}[29]. In the present study, the observed C=C stretching vibrational modes of the title compound are 1607 and 1506 cm^{-1} in experimental FT-IR and also C–C stretching vibrational

Table 1 Detailed assignments of fundamental experimental and theoretical vibrations of AATC by normal mode analysis

Modes	Experimental IR (cm^{-1})	Theoretical Value			Assignments with PED^{d} (%)
		Scaled frequency	Unscaled frequency	I_{IR}^{b}	
1		3691	3543	44.73	ν_{asy}NH (96)
2	3451	3662	3516	12.12	νNH (100)
3		3571	3428	146.89	νNH(96)
4	3358	3561	3417	44.15	νNH(100)
5	3239	3235	3106	2.10	νCH(98)
6		3229	3100	4.10	νCH(84)
7		3220	3091	6.28	νCH(95)
8		3216	3087	27.29	νCH(84)
9		3206	3078	37.66	ν_{asy}CH(88)
10		3193	3065	14.70	νCH(89)
11		3183	3056	23.77	νCH(88)
12		3183	3056	5.87	νCH(88)
13		3180	3053	17.90	νCH(97)
14	2214	2316	2223	124.98	ν_{asy}(90)+νCC(10)
15	1640	1696	1628	204.49	βHNH(42)+τHNCC(10)
16		1681	1614	258.01	βHNH(81)
17		1669	1602	161.01	νCC(57)+βHNH(13)+βHCC(17)
18		1655	1589	2.85	νCC(51)+βHCC(20)
19		1636	1571	1.61	νCC(53)+βHCC(13)
20	1607	1620	1555	16.61	νCC(53)+βHCC(10)
21		1574	1511	35.87	νCC(14)+ν_{asy} CC(12)+β'HCC(29)
22		1559	1497	283.54	ν_{asy}CC(38)+β'HCC(29)
23		1533	1472	15.54	βHCC(52)+βCCC(11)
24		1530	1469	234.23	νCC(57)+ν_{asy} NC(57)+ν_{asy} NN(10)
25	1506	1505	1445	78.24	νCC(11)+νCCC(10)+νNC(10)+βHCC(31)+β'HCC(11)
26		1485	1426	21.88	ν_{asy}(38)+βHCC(10)
27		1461	1403	311.15	νNN(55)
28	1439	1432	1375	434.71	ν^{2}CC(38)+νNN(38)
29		1380	1325	1.23	ν_{asy}(14)+δHNC(13)+βHCC(50)
30		1377	1322	24.04	νCC(15)+νNC(16)+ν_{asy}(11)+ν_{asy}NC(11)+ν_{asy}CC(14)
31		1366	1311	36.89	ν_{asy}(52)+βHCC(18)
32		1349	1295	3.83	βHCC(56)
33		1340	1286	6.88	νCC(39)+βHCC(25)
34	1334	1337	1284	114.75	νNC(60)+βHCC(21)
35	1297	1294	1242	20.03	νNC(11)+νCC(17)+νNC(17)+ν^{2}CC(25)+νNN(25)
36		1240	1190	20.87	ν_{asy}NC(46)+ν_{asy}CC(46)
37		1226	1177	49.48	ν_{asy}CC(20)+βHCC(71)
38		1190	1142	0.79	βHCC(79)
39		1186	1139	0.35	β'HCC(84)
40	1181	1182	1135	40.67	νCC(13),νNC(13),δHNC(27)
41		1172	1125	10.72	ν_{asy}CC(16)+δHNC(11)+βHCC(57)
42		1163	1117	68.89	νNC(20)+δHNC(17)
43		1108	1064	10.05	ν_{asy}CC(17)+ν_{asy}NC(11)+ν_{asy}CC(11)+βHCC(56)
44		1096	1052	1.72	νCC(15)+δHNC(57)
45		1049	1007	3.47	νCC(46)+βHCC(24)+βCCC(17)
46		1032	991	0.15	βHCC(11)+βCCC(70)
47		1015	974	0.13	νCC(27)+βCCC(57)

Table 1 (continued)

Modes	Experimental IR (cm^{-1})	Theoretical Value			Assignments with PED^{d} (%)
		Scaled frequency	Unscaled frequency	I_{IR}^{b}	
48		1000	960	0.38	τHCCC(60)+τCNNC(10)+τCCNN(10)+τRCCCC(10)
49		979	940	0.06	τHCCC(81)
50		963	925	1.17	τHCCN(22)+τHCCC(22)+τHCCN(12)+τHCCC(12)
51		952	914	3.33	τHCCN(60)+τHCCC(60)+τ^{2}HCCN(10)
52		948	910	1.94	τHCCN(61)+τHCCC(61)
53		940	902	3.85	τHCCC(83)
54		919	882	4.16	νCC(11)+νNC(11)+βCNN(48)+βCCC(48)
55		861	827	0.15	τHCCC(99)
56		854	820	4.29	νCC(56)+νNC(56)
57		841	807	46.70	τHCCN(70)+τHCCC(70)
58		821	788	4.39	τHCCC(94)+τHCCN(94)
59		815	782	10.95	νSC(30)+βCCC(11)+βCCN(11)
60		795	763	22.46	βCCN(12)+βCCC(15)+βCCS(15)+τHCCN(13) +τHCCC(13)
61		787	756	26.90	τHCCC(62)+τRCCCC(19)
62		738	709	12.15	τRCCCC(15)+τRCCCC(42)+δNCCC(19)
63	731	717	688	6.59	βCCC(52)+βCNN(52)
64		703	675	25.25	τHCCC(27)+τHCCC(13)+τRCCCC(40)
65		694	666	2.87	δCCCC(25)+τRCCCC(25)+τRCCCC(13)+δCCC(15)
66	690	654	628	1.41	βCCC(63)+βCCC(12)
67		630	605	0.12	βCCC(84)
68		627	602	2.48	δCCCC(13)+τRCCCC(13)+τCCNN(12)+δNCSC(21)
69		602	578	15.46	βCCC(25)+τHNCC(12)
70		569	546	263.01	τHNCC(21)+δNCCC(11)
71		550	528	81.29	βCCC(17)+βCCC(18)+βCCN(18)
72		541	519	40.28	τRCCCC(49)+τCNNC(49)+δNCCC(49)
73		534	513	21.23	βCCC(28)
74		516	495	65.13	βCNN(18)+βNCC(13)
75		512	492	90.44	τHNCC(11)+δNCCC(14)
76		504	484	4.14	τNCCC(56)+δNCSC(21)
77		469	450	22.03	βCCS(56)
78		455	437	18.39	τCCCN(50)+τRCCCC(50)+δCCCC(50)+τCCNN(50)
79		428	411	47.49	βCCC(10)+βCCN(10)+βNCS(10)+τHNCC(38)
80		426	409	42.71	βCCC(14)+βCCN(14)+βNCS(14)+τHNCC(28)
81		421	404	1.41	τHCCC(13)+τRCCCC(67)
82		419	402	6.33	τRCCCC(69)
83		394	378	6.78	βCCN(58)
84		337	324	16.51	τHNCC(79)
85		334	321	8.26	βNCS(12)+βCCN(12)+βCCC(12)+βCCS(12)
86		320	307	283.19	βNCS(12)+βCCN(12)+βCCC(12)+βCCS(12)
87		311	299	6.01	τHNCC(76)
88		294	282	7.99	τCNNC(61)+τCCNN(61)+τRCCCC(61)+τCCNN(10)
89		274	263	7.34	νCC(19)+βCCC(16)
90		246	236	2.16	βCCC(11)+βCCS(11)
91		226	217	3.38	τCCNN(23)+τRCCCC(23)+δNCCC(23)+τCNNC(23)
92		182	175	7.82	βNCC(12)+βCCC(11)+τRCCCC(24)
93		173	166	1.69	βCCC(36)+βCNN(36)+βNCC(10)
94		145	139	1.11	τCCNN(10)+τRCCCC(10)+δNCCC(10)

Table 1 (continued)

Modes	Experimental IR (cm^{-1})	Theoretical Value			Assignments with PED^{d} (%)
		Scaled frequency	Unscaled frequency	I^{b}_{IR}	
95		133	128	4.19	βCCC(65)+βCCN(65)
96		115	110	0.83	δCCCC(18)
97		83	80	2.98	βCCC(10)+βCCS(10)+βCCC(14)+τCCCC(10)
98		64	61	4.58	τRCCCC(63)
99		61	59	3.30	τRCCCC(55)+δCCCC(65)
100		40	38	0.33	τCCCN(63)+τCCNN(63)+τCNNC(63)
101		34	33	0.09	βCNNC(17)+βCCN(19)+βCCC(11)+τCCNN(19)
102		32	31	0.07	τCCNN(45)

$v = symmetricalstretching, v_{asy} = asymmetricalstretching, \beta = inplanebending, \delta = outofplanebending, \tau = torsional, \tau R = torsionalring,$

modes are assigned at 1297 and 1181 cm^{-1} respectively in experimental FT-IR. The C–C–C planar vibration wave number will be reported in the range of 999–665 cm^{-1} by Sarojini and Co-workers [30]. The experimental aromatic ring C–C–C bending vibrations of the title compound has appeared at 731 and 690 cm^{-1} in experimental FT-IR. The computationally calculated FT-IR for C=C stretching vibrations, C–C stretching vibrations, and aromatic ring C–C–C bending vibrations are 1602 and 1411 cm^{-1}, 1286 and 1190 cm^{-1}, 763 and 688 cm^{-1}, respectively.

3.2 Electron Spray Ionization (ESI) GC–MS Analysis

A method that enables the determination of a compound's molecular weight (mass) is mass spectrometry. Furthermore, it is possible to learn important structural details about the unidentified entity by calculating the masses of the pieces formed when high-energy molecules collide [31]. The mass spectrum of a chemical is often displayed as a bar graph with intensity (the number of ions of a certain m/e striking the detector) on the y-axis and m/e values (unit masses) on the x-axis. Gas chromatography-mass spectrometry (GC–MS) is a hyphenated technology that combines the detention power of mass spectrometry with the separating capacity of gas chromatography (GC). The molecular formula of the compound is 529 g/mol. As depicted in Fig. S2 of the supporting information, the mass spectra of the compound gave mass to charge ratio 75, 92, 211, 214, 228, 242, 283.2, 286.9, 301.1, 451.3, 505 correspondings to fragments C_6H_4, C_6H_6N, $C_2H_4S_2O_6$, $C_{11}H_8N_5S$, $C_8H_4S_2O_6$, $C_8H_8S_2O_6$, and $C_{14}H_8S_2O_6N$,

3.3 Natural Bond Orbital (NBO) Analysis

The molecular orbital energies and occupancies of the title molecule is calculated using B3LYP method and 6-311++G(d,p) basis set and the results is presented in Table 2. The second-order stabilization energy in line with the electron delocalization between the filled and unfilled orbitals is calculated as [32, 33].

$$E^{(2)} = \Delta E_{i,j} = -q_i \frac{F^2(i,j)}{\varepsilon_i - \varepsilon_j} \tag{1}$$

To estimate the delocalization patterns of electron density from the main occupied Lewis-type orbitals to unoccupied non-lewis type orbitals, the AATC compound's NBO analysis is performed [34]. Intermolecular charge transfer (ICT), which results in the stability of the molecule, is caused by orbital overlap between bonding C–C, C–N, C–H, N–N, and C–S, according to NBO analysis of the investigated compound. The intramolecular interactions result in high electron density (ED) approximation of antibonding pi (π^*) orbitals. The greatest intramolecular interaction for the studied compound is formed by the orbital overlap between πC3–C4 and π*N16–N17 with electron density 1.725e to 0.009e which results in intermolecular charge transfer (ICT) causing stabilization of the system. The intramolecular hyper conjugative interaction of πC3–C4 to π*N16–N17 leads to the highest stabilization of 27.16 kJ/mol. The electron delocalization from π*C3–C4 to π*C6–C8, π*C1–C2 to π *C3–C4, π*N16–N17 to π*C3–C move with very high stabilization energy of 87.35, 86.37, and 47.81 kJ/mol respectively. Significant resonance interactions were observed LP (1) N29 to π*C1–C2, LP (1) N34 to π*C11–C13, LP (2) S5 to π*(2) C1–C2 show stabilization energies of 44.07, 28.60, and 27.37 kJ/mol with electron densities of 1.752e to 0.455e, 1.828e to 0.408e and 1.693e to 0.455e are also highly responsible for the stability of the studied compound.

Table 2 Representative values of Natural bond orbital (NBO) analysis for the studied compound

Donor NBO (i)	ED(e)	Acceptor NBO (j)	ED (e)	E(2)kcal/mol	E(j)-E(i), a.u	F(I,j) a.u
πC1–C2	1.96	π*C1–C2	0.38596	20.49	0.30	0.073
πC1–C2		π*C32–N33	0.11525	22.58	0.38	0.087
πC3–4	1.73	π*C1–C2	0.45518	1.35	0.26	0.051
πC3–C4		π*N16–N17	0.00894	27.16	0.25	0.074
πC6–C8	1.63742	π*C3–C4	0.38596	6.23	0.26	0.058
πC6–C8		π*C7–C9	0.31067	22.41	0.02	0.072
πC6–C8		π*C11–C13	0.40825	17.28	0.27	0.062
C7–C9	1.71642	π*C6–C8	0.40622	15.00	0.29	0.060
C7–C9		π*C11–C3	0.40825	22.28	0.073	0.073
C11–C13	1.61076	π*C6–C8	0.02294	25.75	0.28	0.077
C11–C13		π*C7–C9	0.01253	15.18	0.29	0.060
N16–N17	1.89354	π*C3–C4	0.38596	13.30	0.37	0.068
C18–C20	1.68344	π*N16–N17	0.00894	23.04	0.21	0.063
C19–C21	1.68344	π*C18–C20	0.38392	19.25	0.28	0.067
C23–C25	1.6594	π*C18–C20	0.38392	0.28	0.28	0.069
LP(2)S5	1.69313	π*C1–C2	0.45518	27.37	0.24	0.076
LP(1)N16	1.90698	π*C4–S5	0.08757	6.32	0.55	0.085
LP(1)N29	1.75171	π*C1–C2	0.45518	44.07	0.29	0.107
LP(1)N33	1.96878	RY*(1)C32	0.01934	16.57	1.15	0.123
LP(1)N34	1.82838	C11–C13	0.40825	28.60	0.33	0.092
C1–C2	0.45518	C3–C4	0.38596	86.37	0.03	0.070
C3–C4	0.38596	C6–C8	0.40622	87.35	0.02	0.059
N16–N17	0.34595	C3–C4	0.03014	47.81	0.04	0.068

From the full NBO analysis in Table S2 of the supporting information, the high value of occupancies is predicted for CR(N93), CR(N34), CR(N17), CR(C32), CR(N16), CR(S5) bonding and its values are 1.99964, 1.99949, 1.99948, 1.99938, 1.99935, 1.99933. Therefore, the results suggest that CR(N93), CR(N34), CR(N17), CR(C32), CR(N16), CR(S5) bonding are essentially controlled by the p-character of these hybrid orbitals. The information found in Table S2 of the supporting documentation demonstrates that the ring and substituted groups interact (σ→σ^*) intramolecularly in a hyper conjugative manner. The occurrence of a few σ→σ^* transitions between rings and substituted groups demonstrates the strength of the relationship and further highlights how the chemical characteristics of the substituent and ring can be combined [35, 36]. The outcome of NBO study has supported the biological activity of the APTC.

3.4 Hole-Electron Excitation Analysis

Here, the movement of an electron from the hole to the electron is the main focus, and both the electron and the hole are depicted as real space functions. It should be emphasized that determining if a transition mode is a local excitation can be done using the overlapping integral of the hole-electron distribution. The charge transfer length of the current electron distribution mode is determined by the distance between the centroid of the hole and electron. The t, S r, and D indices, respectively, show whether the electron and hole distributions overlap, how much they overlap, and the magnitude of the charge transfer length overlap. The hole and electron are not regarded as separated due to charge transfer when $t < 0$, in accordance with [37–41], who state that "The t index measures the separation extend of the hole and electron in charge transfer (CT) direction." The positive t index relates to the separation of the hole and electron distributions. In this section, excitation parameters: Hole-electron length (D) which can be considered as the charge transfer excitation, the overlap function (S_r), the H index which reflects the breadth of the average distribution of hole and electron, the t index corresponds to the degree of hole and electron separation, the hole-electron coulomb attraction energy (E_{cou}), hole delocalization index (HDI), and electron delocalization index (EDI) of all the five excited states are calculated and presented in Table 3. The hole delocalization index and electron delocalization index are both included in the table. S0→S3 and S0→S4 for the D index had extremely high values of 2.62 Å and 3.27 Å, respectively. As a result, they are thought of as CT excitations. The Sr indices of the five excitations are seen to be relatively large in Table 3. Because the excitation is of the highly confined π^* kind, the value of Sr for excited state 2, or S0→S2, is fairly high up to 0.71. S0→S1 is a n–π^*

Table 3 Electron Excitation analysis of the five excited states of ACDP

	D(Å)	Sr	H(Å)	t(Å)	E_{coul}(eV)	HDI	EDI
S0→S1	0.70	0.50	2.42	−0.87	5.03	15.33	8.47
S0→S2	1.13	0.71	3.38	−0.97	0.14	6.35	8.68
S0→S3	2.62	0.53	3.36	0.57	3.34	6.48	8.54
S0→S4	3.27	0.55	2.70	1.38	3.18	8.03	7.31
S0→S5	1.48	0.58	3.53	−0.82	2.69	4.84	4.65

kind of excitation, which explains why its Sr value (0.50), which is tiny in comparison to the CT excitations of S0→S3 and S0→S4, is highly localized. All five types of excitations have substantial values for the H-index, which measures the width of the average distribution of holes and electrons, but the excitations from S0→S2, S3, and S5 have the highest values. The hole electron map reveals that the distribution of the hole and electron of S0S1 is localized. The separation of the hole and electron is evident, according to the S0–S3–S4 t indices, which are somewhat positive. Therefore, it is crucial to think of S0→S3, S4 as CT excitations. It is also reasonable to infer from the t value that the excited state S0→S4 experiences more charge transfer than S0→S3. The fact that the t indices for excitations S0, S1, S2, and S5 are all negative values shows how little their hole and electron are separated from one another. As shown in the table, it is clear that the electron of the excited state S0→S1 is only somewhat localized despite having a reasonably high value of EDI, whereas the hole of the same excited state is very localized due to the high value of HDI. The excited state S0→S1 is strongly confined when comparing the HDI and EDI values of all excitations. In contrast, S0→S2, S3, S4, and S5 have higher delocalized electron and hole distributions. This is brought on by their low HDI and EDI levels. The least amount of HDI and EDI is visible in the excited state S0→S5. The Sr index should, obviously, be the most significant in these investigations given the link between the hole-electron Coulomb attractive energy and the other electron excitation properties. It is clear that the main effect of the Sr index is the distance.

Distributions between the hole and electron which decreases the Coulomb attractive energy. The Sr value of S0→S2 is the highest, while having the least Coulomb attractive energy, whereas the Sr value of S0→S1 has the highest Coulomb attractive energy. Between the highest and lowest Coulomb attractive energy are shown by other excitations.

3.5 ADCH Population Analysis

The values are presented in Table S1 of the supplementary information. ADCH is calculated using the Multiwfn software analyzer using output from Gaussian 09 using the B3LYP method with 6-311++G(d,p) basis set. High efficiency and basis set insensitivity characterize the Hirshfield population analysis [42]. A better variant of the Hirschfield charge is ADCH [43]. The name ADCH comes from the fact that it is a modified version of the Hirschfield charge. By addressing the low dipole moment repeatability that exists in the Hirschfield charge, it enhances it. Due to the atomic charge effect, molecular polarizability, biological activity, and other molecular features that define a system, ADCH analysis is crucial in the application of quantum chemical calculations to the molecular system. Because electronegative hydrogen (less positive) is present, the carbon atom pulls the positive charge from the nitrogen atom, giving C32 the highest positive atomic charge of all the carbon atoms, according to the results of the ADCH analysis. As a result, C32 is the most acidic carbon atom and is vulnerable to nucleophilic assault. The presence of electronegative nitrogen allows the hydrogen atom to attract the positive charge from the nitrogen atom, making the H30 more electrophilic than the other hydrogen atoms, according to the ADCH atomic charge of the examined molecule. The additional hydrogen atoms that are immediately connected to nitrogen are also in this situation; their ADCH charges are also very positive. The N29 and N34 atoms in the modeled structure have larger negative atomic charges than the other atoms, according to the ADCH. The large positive values of the carbons linked to the electronegative nitrogen are readily apparent from Table S1. The total charge of the atoms that make up a fragment is known as the fragment charge. A ring is more acidic the higher its positive charge. Furthermore, fragment 3 has the most population and the largest positive charge value. As a result, the acidic ring is fragment number three. The population value and about equal amounts of negative charge are shared by fragments 1 and 2. The two end rings each have a negative atomic charge, while the centre ring has a large positive charge.

3.6 Frontier Molecular Orbitals (FMOs)

The energy of the frontier molecular orbitals is crucial for identifying a number of factors that influence a molecule's stability and reactivity. The concept of FMOs can be used to characterize all of a molecule's global reactivity properties. By deducting the energy of the LUMO from the HOMO (E HOMO-E LUMO) in FMOs, the energy band gap can be used to characterize crucial molecular characteristics as stability, reactivity, hardness, and non-linear optical properties [44, 45]. The bioactivity of the molecule will be described by the energy band gap value. A smaller band gap indicates strong molecular interaction and therefore ICT within the molecule. This in turn is used to predict the bioactivity of the molecule. The isosurface of the E_{HOMO}, E_{LUMO}, E_{LUMO+1}, E_{HOMO-1}, $E_{HOMO} - E_{LUMO}$, $E_{HOMO-1} - E_{LUMO+1}$ for the AATC studied structure were calculated by DFT/B3LYP method with 6-311++G(d,p) basis set are shown in Fig. 2. From the analysis of FMOs 375 molecular orbitals were identified for the structure. Of the 375 MOs 83 were occupied and the rest were unoccupied. Out of these 82, 83, 84, and 85 are the HOMO-1, HOMO, LUMO, and LUMO + 1 respectively. Their corresponding energy values are − 5.8 eV, − 5.2 eV, − 2.2 eV, − 0.5 eV. Calculating the energy band gap values between HOMO and LUMO of the modeled structure, we obtain 2.95652 eV as the value for the energy band gap of the structure. The low value of the band gap indicates the biological activity of the studied compound. The energy band gap has a very interesting relationship with NLO. Therefore, the low value of $\left(E_{HOMO} - E_{LUMO}\right)$ for the studied compound also indicates the presence of the NLO effect. The band gap of $E_{HOMO-1} - E_{LUMO+1}$ was obtained to be 5.26486.

3.7 Molecular Electrostatic Potential (MESP)

The electrostatic potential is plotted on the surface of constant electron density in the MESP. A quantum-molecular descriptor called the molecular electrostatic potential is utilized to detect or locate molecular locations that could be vulnerable to nucleophilic and electrophilic assaults [46, 47]. The MESP is crucial for understanding how hydrogen bonds and a molecule's charge distribution interact. The following equation was used to determine the MEP for the structure under study:

$$V(r) = \sum Z_A/(R_A - r) - \int \rho(r')/(r' - r)dr' \tag{2}$$

where the summation runs over all the nuclei A in the compound. Z_A is the charge of the nucleus A, located at R_A and $\rho'(r)$ is the electron density function of the molecule. Different colors are used to illustrate various electrostatic potential levels. Deepest red denotes regions that are highly nucleophilic (electron-rich), deepest blue denotes regions that are highly electrophilic (electron-poor), light blue denotes regions that are slightly electron-deficient, yellow denotes regions that are slightly electron-rich, and green denotes neutral regions.

The color code of our present esp map is from − 6.985 $\times 10^{-3}$ (deepest red) to 6.985 $\times 10^{3}$ (deepest blue) for the studied compound as displayed in Fig. 3. MESP of the studied compound shows that the highest nucleophilic regions are around N33, − 0.0285171 of Cyanide group, N16, − 0.0209126 (which was predicted by CDD as the most nucleophilic region for attack by electrophiles), and N17, − 0.01285 of the azo group. Also, S5 of the thiophene is a rich electron site. The MESP map also shows that the two amino groups constitute the highest electrophilic deficient regions. H36 (0.0407641), H30 (0.0357419), and N34 (0.0291402) constitute the highest points for attack by nucleophiles.

3.8 Conceptual Density Functional Theory

The CDFT was applied as quantum chemical tool to vividly describe the global reactivity of the title molecule as reported in Table S2 of the supporting information. In this study, to calculate global reactivity descriptors such as molecular orbital energies (HOMO and LUMO), energy gap (ΔE), electron affinity (EA), ionization potential (IP), Chemical potential (μ), chemical hardness (η), Softness (σ), electronegativity (γ) and electrophilicity index (ω), the Koopman's approximation was employed.

$$\text{VIP} = -E_{HOMO} \tag{3}$$

$$\text{VEA} = -E_{LUMO} \tag{4}$$

$$\chi = \frac{(VIP + VEA)}{2} \tag{5}$$

$$\mu = -\frac{-(VIP + VEA)}{2} \tag{6}$$

$$\eta = \frac{VIP - VEA}{2} \tag{7}$$

$$\sigma = \frac{1}{\eta} \tag{8}$$

$$\omega = \frac{\mu^2}{2\eta} \tag{9}$$

From the result obtained, the hardness value was 1.5045 eV, which suggests more reactivity and possibility of Intramolecular charge transfer. The calculated value of electronic chemical potential (μ), softness (σ), electronegativity (γ) and electrophilicity index (ω) are − 3.70633 V, 0.6647 eV^{-1}, 3.7063 eV, 4.5652 eV respectively. According to literature [48], the chemical reactivity parameters indicate that ACDP molecule is biologically active.

Electrophilicity index encompasses the tendency of an electrophile to acquire an extra amount of electron density and the resistance of a molecule to exchange electron density with the environment [49]. The electrophilicity scale ω scale allowed the classification of organic molecules as strong electrophiles with $\omega > 1.5$, moderate electrophiles with $0.8 < \omega < 1.5$ eV and marginal electrophiles with $\omega < 0.8eV$ [49]. Since ω of the studied structure is 4.5652 eV. Hence, it is a strong electrophile and shows high biological activity.

3.9 Local Reactivity Descriptors

The reactivity of each atom in a molecule is predicted using local reactivity descriptors. The Fukui function and the dual descriptor are two of the most significant subgroups of these reactivity descriptors. In more recent study, Martinez–Araya has discussed [50] the suitability of using a condensed relationship rather than the nucleophilic and electrophilic Fukui functions in the Hirsfeld population analysis for predicting preferred reaction sites. The relation provides the Fukui function.

$$f(r) = \left[\frac{\partial\rho(r)}{N}\right]_v \tag{10}$$

where N is the number of electrons in the present system, the constant term v in the partial derivative is external potential. Fukui function can be defined for three situations:

$$\text{Nucleophilic attack } f^+(r) = \rho_{N+1}(r) - \rho_N(r) \tag{11}$$

$$\text{Electrophilic attack } f^-(r) = \rho_N(r) - \rho_{N-1}(r) \tag{12}$$

$$\text{Radical attack } f^0(r) = \frac{f^+(r) + f^-(r)}{2} \tag{13}$$

The electrophilic Fukui function, f^+(r), describes the reactive sites in a molecule that are susceptible to nucleophilic attack, and the nucleophilic Fukui function, f^-(r) describes the reactive sites that are more susceptible to electrophilic attack. The radical Fukui function $f^0(r)$, which is the average of $f^-(r)$ and $f^+(r)$ denotes the favorable site for radical attack. The condensed dual descriptor, $\Delta f(r)$ is a very important parameter to study reactive sites. It is mathematically represented as:

$$\Delta f(r) = \left(\frac{\partial f(r)}{\partial N}\right)_{v(r)} = f^+(r) - f^-(r) \tag{14}$$

The sites in a molecule that are more vulnerable to electrophilic assault and nucleophilic attack can be identified using CDD. The most reactive locations in the structure under study are predicted in this situation using CDD. The location is favorable for nucleophilic assault if CDD > 0 and advantageous for electrophilic attack if CDD 0. According to Table S3 of the supporting data, C3 has the highest positive CDD value of any carbon atom. the most advantageous location for a nucleophilic assault on carbon atoms. The atom in the named compound, N16, has the highest positive CDD value of all the atoms, making it the location that is most vulnerable to nucleophilic assault. For both carbons and other atoms, C4 has the largest negative CDD value. It is therefore the location where entering nucleophiles are most likely to engage in electrophilic assault. Figure 4a–c of the supporting information gives the isosurface of f^-,f^0 and CDD respectively for the reduced compound. In the map in Fig. 5c, green and blue isosurface correspond to positive and negative region of CDD, respectively. Clearly, most negative part of CDD function is localized on C4, N29, C2, C8, C11, C9, N34. Hence, these positions are favorable reactive sites for electrophilic attack. The most positive part of CDD function is localized on C1, C3, C8, C7, N16, N17. These positions are favorable sites for nucleophilic attack.C32, C13, C19, C21, C23 are not so positive as C1, C3, C8, C7, N16.

3.9.1 Aromaticity Index

Para Delocalization Index is a theory used to calculate the aromaticity indices of a six-membered ring [51]. PDI is defined as the average of the sum of the delocalization index in a six-membered aromatic ring [52]. For a C1–C6 membered benzene ring it is mathematically represented as:

$$PDI = \frac{\delta(1,4) + \delta(2,5) + (3,6)}{3} \tag{15}$$

It has been found that the delocalization and aromaticity increase with increasing PDI. It can be seen from Table 1 that fragment 2 has the bigger PDI. They are primarily delocalized and fragrant as a result. Similar to PDI, FLU is another aromaticity index that may be determined for aromatic rings of any number of atoms [53]. FLU is mathematically represented as:

$$FLU = \frac{1}{n}\sum_{A-B}^{ring}\left[\left(\frac{V(B)}{V(A)}\right)^{\alpha}\frac{\delta(A,B) - \delta_{ref}(A,B)}{\delta_{ref}(A,B)}\right]^2 \tag{16}$$

where the summation runs over all adjacent pairs of atoms around the ring, n is equal to the number of atoms in the ring, δ_{ref} is the reference DI value, which is a pre calculated parameter, α is used to ensure the ratio of atomic valences is greater than 1.

$$\alpha = \begin{cases} 1 V(B) > V(A) \\ -1 V(B) \leq V(A) \end{cases} \tag{17}$$

From Eqs. (16) and (17), it is obvious that the lower the FLU value the higher the aromaticity since FLU can be carried

Table 4 (a) Aromaticity indices showing PDI, PLR, FLU, FLU-π

PLR	PDI	FLU	FLU-π
Fragment 1 (0.4932)	0.0829	0.0055	0.0109
Fragment 2 (0.5468)	0.0911	0.0030	0.0276

Table 4 (b): Aromaticity indices showing HOMA and BIRD analysis

Fragments	HOMA	BIRD
Fragment 1	0.9323	91.6056
Fragment 2	0.9608	94.7305
Fragment 3	0.4954	49.1483

out for rings with any number of atoms. The aromaticity parameters of the studied compound are shown in Tables 4a, 4b. Fragment 3 which corresponds to a ring with five atoms that has the least FLU value becomes the most aromatic and delocalized. Therefore, according to FLU Frag 3 < Frag 2 < Frag 1.

Flu-π is based on DI−π and π−atomic valence [54]. It is mathematically represented as

$$FLU_{\pi} = \frac{1}{n}\sum_{A-B}^{ring}\left[\left(\frac{V_{\pi}(B)}{V_{\pi}(A)}\right)^{\alpha}\frac{\delta_{\pi}(A,B)-\delta_{ref}(A,B)}{\delta_{ref}(A,B)}\right]^{2} \tag{18}$$

Similarly, like FLU, the lower the FLU_{π} the higher the aromaticity in the compound. From Table 1 Fragment 1 has the least FLU_{π} value, hence, the most aromatic.

PLR is PDR with DI replaced by CLRK [55]. It is mathematically represented as:

$$PLR(A,B) = \frac{\chi_{1,4}+\chi_{2,5}+\chi_{3,6}}{3} \tag{19}$$

PLR like PDI has stronger aromaticity with higher values of PLR. Therefore, Fragment 2 has the strongest aromaticity.

HOMA is another theory for studying aromaticity indices [56]. It is represented by the formula:

$$HOMA = 1 - \sum_{i}\frac{\alpha_{i,j}}{N}\left(R_{ref}-R_{i,j}\right)^{2} \tag{20}$$

where N is the number of atoms considered, j denotes the atom next to atom i, α and R_{ref} are pre-calculated constants given in the original paper for each type of atom pair. From Eq. (20), it is possible to deduce that if HOMA equals 1 the ring is fully aromatic, and if HOMA equals 0 the ring is not aromatic. From Tables 4a, 4b it is obvious that fragment 2

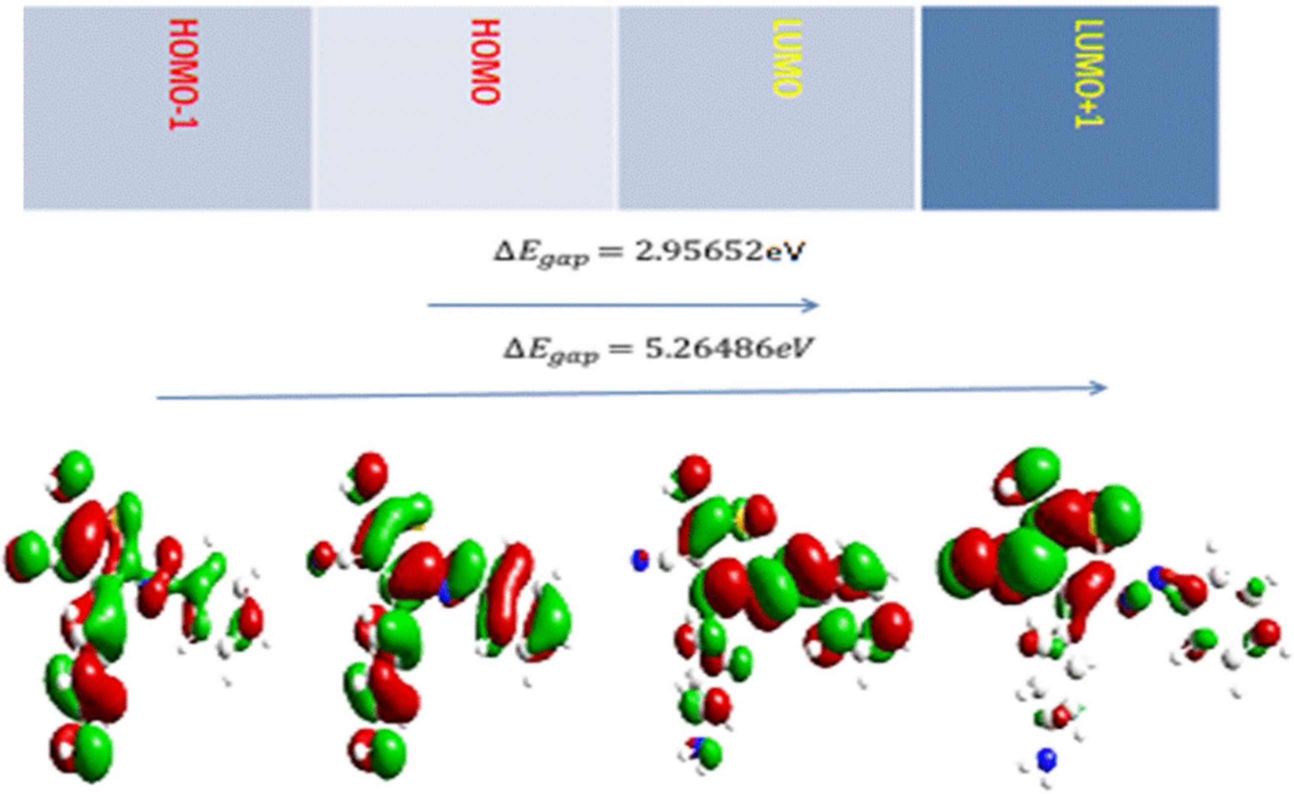

Fig. 2 Molecular orbital and energies for the HOMO, LUMO, HOMO − 1, LUMO + 1 of the modeled structure (AATC)

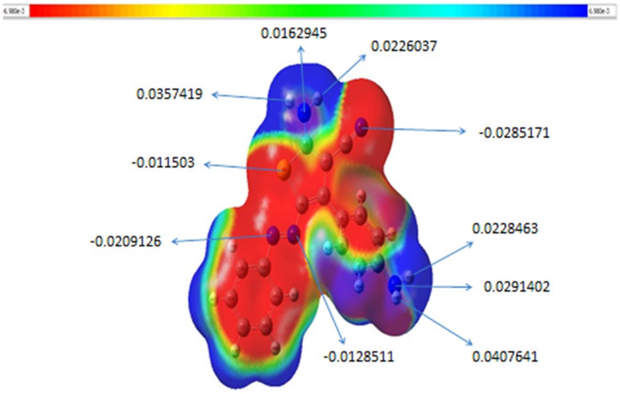

Fig. 3 Molecular electrostatic potential map calculated at B3LYP/6-311++G(d,p) level

is the most aromatic since it has the highest HOMA value. Hence, Frag 2 < Frag 1 < Frag 3.

BIRD is a geometry-based theory that can also be used to study the aromaticity of rings [57]. It can be represented by the following formula:

$$I = 100\left[1 - \left(V/V_K\right)\right] \tag{21}$$

$$V = \frac{100}{N}\sqrt{\frac{\sum_i \left(N_{i,j} - \overline{N}\right)^2}{n}} N_{i,j} = \frac{a}{R_{i,j}} - b \tag{22}$$

i cycle all of the bonds in the ring, j represents the atom next to atom I, n is the total number of bonds considered. N represents Gordy bond order, $\overline{N}$ is the average value of the N values. $R_{i,j}$ Represents the bond length, a and b are predefined parameters respectively for each type of bond. According to the equation in Eq. (21), the more the BIRD index is close to 100, the more aromatic the matching ring is. Additionally, BIRD supports the higher aromaticity of ring 2 that HOMA analysis has already suggested. In conclusion, it is seen that, of the six criteria examined for aromaticity, five confirmed the greater and stronger aromaticity of frag 2, with the exception of the FLU analysis, which suggested that frag 3 would have greater aromaticity. This might be caused by the fewer atoms in ring of fragment 1.

3.9.2 Non-Linear Optical (NLO) Effects

The nonlinear response of variables like frequency, amplitude, phase, or other propagation characteristics of incident fields is explained by nonlinear optical (NLO). On the other hand, nonlinear optical (NLO) effects result from interactions between applied electromagnetic radiation to create new fields from incident one [58]. According to P. N. Prasad and D. J. Williams, organic materials with high levels of electron donors and acceptors as well as highly delocalized π-electron portions of molecules are excellent sources of NLO materials [59]. A Taylor's series expansion of the total dipole moment, μ_tot, caused by the electric fieldE i (ω) can be used to represent the NLO response of an isolated molecule in the field.

$$\mu_i\left(E_i\right) = \mu_i + \alpha_{ij}E_j + \frac{1}{2!}\beta_{ijk}E_jE_k + \frac{1}{3!}\gamma_{ijkl}E_jE_kE_l + \ldots$$

where E_i be the homogenous electric field, $\mu_i(E)$ be the dipole moment in an electric field, μ_i be the dipole moments at zero field, $\alpha_{ij}, \beta_{ijk}, \gamma_{ijkl}$ are the polarizability tensor component, first-order hyperpolarizability component, and second-order hyperpolarizability component, respectively. The electric dipole moment (μ) and the average polarizability (α_{tot}) using the x, y, and z components can be obtained by the following relation:

$$\mu = \sqrt{\left(\mu_x^2 + \mu_y^2 + \mu_z^2\right)}$$

$$\alpha_{tot} = \frac{\alpha_{xx} + \alpha_{yy} + \alpha_{zz}}{3}$$

Anisotropy of polarizability

$$\Delta\alpha = 2^{-1/2}\left[\left(\alpha_{xx} - \alpha_{yy}\right)^2 + \left(\alpha_{yy} - \alpha_{zz}\right)^2 + \left(\alpha_{zz} - \alpha_{xx}\right)^2\right]^{1/2}$$

The first order polarizability (β_{ijk}) is a 3^{rd} rank tensor ($3 \times 3 \times 3 matrix$). the equation for calculating the magnitude of first-order hyperpolarizability i

$$\beta_{tot} = \sqrt{\beta_1^2 + \beta_2^2 + \beta_3^2}$$

where

$$\beta_i = \frac{1}{3}\sum_{j=1}^{3}\left(\beta_{ijj} + \beta_{jij} + \beta_{jji}\right) = \sum_{j=1}^{3}\beta_{ijj}$$

Here i, j = x, y, and z. and the final form resulting from Kleinman symmetry [60].

Polar keyword, B3LYP functional, and 6-311++G (d,p) basis set were used in the computations, and the output was loaded using a multiwave function analyzer. The results are all reported in a.u. Table 5's findings include the electronic atomic dipole moment, average polarizability that is isotropic, polarizability anisotropy, and initial hyperpolarizability's magnitude. The predicted dipole moment in this investigation is 0.607926 au. The maximum value of the dipole moment is observed along the z-direction – 0.470857 au. The calculated average polarizability (α_{tot}) and anisotropy of polarizability value are 293.8313 au and

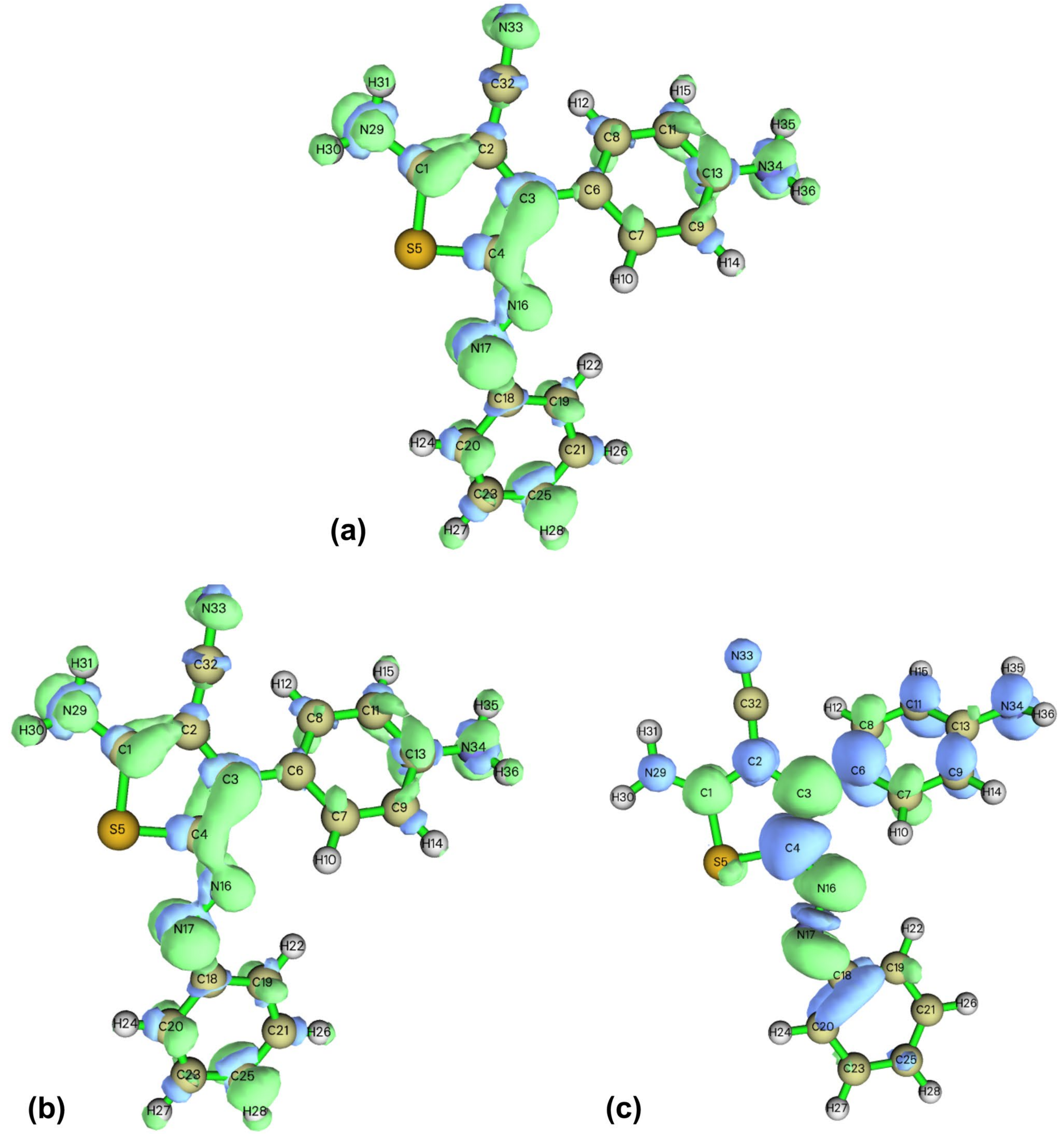

Fig. 4 **a** Isosurface map of f^{-} for AATC. **b**: isosurface map of f^{0} for AATC**. c**: isosurface map of CDD for AATC

296.1043, respectively. According to Table 5, the examined chemical has a first-order hyperpolarizability value of 3993.12069 atomic units. Average polarizability and first-order hyperpolarizability values calculated are much higher than those for urea (β_tot = 43au) [61], a reference molecule for analyzing NLO response. The reduced molecule is found to have a first hyperpolarizability value that is 93 times greater than that of urea, making it a strong contender for use as an NLO material and a desirable subject for future research on its non-linear optical properties.

3.9.3 Pharmacological Investigation

The characteristics of the examined substance and the test drug sample, isozianid, employed in this study are described in Table 6. The Lipinski RO5 explained four physicochemical parameter ranges (MWT $\le$ 500, miLogP $\le$ 5, No. of H-bond donor $\le$ 5, No. of H-bond acceptors 10) and offered information on the orally active medicines. When compared to isozianid, the physicochemical parameter values of the aforementioned compound follow the Lipinski RO5 (Rule of 5) without any appreciable divergence.

Log P^a: Logarithm of the partition coefficient between n-octanol and water (miLogP).

$TPSA^b$: Topological polar surface area.

MW^c: Molecular weight.

n rot b^d: Number of rotatable bonds.

Using the pkCSM web server model, the ADMET absorption, distribution, and hazardous characteristics for the named chemical and isozianid have been calculated and are shown in Tables 7a, 7b, 7c in the appropriate order. The investigated structure has a higher Caco-2 permeability than isozianid. As a result, the named component will work best for enhancing drug absorption when taken orally. In the small intestine, APTC and isozianid are both heavily absorbed, but the investigated structure absorbs more. It further demonstrates the named structure's favored suited for aiding in the absorption of medicines taken orally. ($-6 \le \log S \le 0.5$) is the suggested range for a chemical to be good oral bioavailability. The examined substance and isozianid adhere to the rule. An ATP-binding cassette called P-glycoprotein serves as a biological barrier by pushing several foreign chemicals out of cells. Isoniazid functions differently to APTC, which can act as a P-gp substrate. Skin

Table 5 The electric dipole moment (μ), polarizability ($\Delta\alpha$), and first order hyper polarizability (β) of reduced compound by B3LYP/6-311++G(d,p) approach and Multi wave function analyzer

Parameter	Value (au)	Parameter	Value (au)	Parameter	Value (au)
μ_x	0.381220	α_{xx}	314.05400	β_{xxx}	2018.93000
μ_y	−0.032930	α_{xy}	21.67440	β_{xxy}	−2038.11000
μ_z	−0.470857	α_{yy}	395.44200	β_{xyy}	−66.60520
μ_{total}	0.607926	α_{xz}	36.74050	β_{yyy}	−584.57000
		α_{yz}	−142.83800	β_{xxz}	1364.49000
		α_{zz}	171.99800	β_{xyz}	−376.10000
		α_{tot}	293.83133	β_{yyz}	219.92800
		$\Delta\alpha$	296.10423	β_{xzz}	395.26700
				β_{yzz}	−132.96500
				β_{zzz}	100.88500
				β_{tot}	3993.12069

Table 6 Molinspiration property values of studied compound (APTC) and isozianid

Compound rot b^d	Mi Log P^a	$TPSA^b$	MW^c	No of H-bond acceptors	No of H-bond donors	No of violations	volume	n atoms	n
APTC	4.00	100.57	319.39	6	2	0	276.11	23	3
Isozianid	−0.97	68.01	137.14	3	2	0	122.56	10	1

Log P^a: Logarithm of partition coefficient between n-octanol and water (miLogP)

$TPSA^b$: Topological polar surface area

MW^c: Molecular weight

n rot b^d: Number of rotatable bonds

Table 7 (a) Computed Absorption properties using pkCSM web server model

Compound	Intestinal absorption			P-gp	
	Caco2 permeability (log P_{app} in 10^{-6} cm/s)	(human) (% Absorbed)	Water Solubility (LogS)	Substrate (Yes/No)	Skin permeability (log kp)
APTC	0.89	97.35	−5.033	Yes	−2.80
Isozianid	0.63	75.65	−0.641	No	−3.17

Table 7 (b) Computed Distribution properties using pkCSM web server model

Compound	V_{Dss}(human) (log L/kg)	Fraction unbound (human)	Blood–Brain–Barrier permeability (c.brain/c.blood)	Central Nervous System permeability (Log PS)
APTC	0.005	0.012	−0.452	−1.603
Isozianid	−0.432	0.635	−0.117	−3.022

Table 7 (c) Computed Toxicity properties using pkCSM web server model

Compound	Oral rat acute toxicity (LD50)	AMES toxicity	Maximum tolerated dose (Human)	Oral rat chronic toxicity (LOAEL)	Hepatotoxicity	Skin sensitisation
APTC	2.714	Yes	0.389	0.764	No	No
Isozianid	2.364	Yes	1.286	2.824	No	No

permeability refers to a substance's capacity to pass through the skin. If a substance has logKp > −2.5, it is thought to have a relatively poor skin permeability. Consequently, APTC is less skin impermeable than isoniazid.

The more a medicine is dispersed in tissue as opposed to plasma, the larger its steady-state volume of distribution (VDss). Low VDss is defined as (log VDss < −0.15), and high VDss is defined as (log VDss > 0.45). As a result, it may be inferred from the values of log VDss that isoniazid is more widely dispersed in plasma than in tissue, whereas the titled molecule is more evenly distributed between the two. The extent to which a medicine attaches to proteins can have an impact on how effective it is since the more tightly it is attached, the less effectively it can diffuse. Isoniazid is less efficient at binding proteins than APTC. To help prevent side effects and toxicities or to increase the effectiveness of medications whose pharmacological activity is within the brain, the ability of a drug to pass into the brain is a crucial characteristic to take into account. Molecules with log BB −1 are poorly distributed to the brain, whereas those with log BB > 0.3 are thought to be ready to cross the BBB for a given substance. The BBB < −1 of the named compound and isoniazid are seen to be neither high nor low, while isoniazid has a higher BBB. Compounds with a Log PS > −2 are considered to penetrate the central nervous system while those with Log PS < −3 are considered as unable to penetrate the CNS. From the values of Log PS in Table 7b, it is observed that titled compound can penetrate the CNS while isoniazid can't penetrate the CNS.

The Oral Acute toxicity (LD50) value for the studied structure is somewhat higher than that of the standard drug implying that the titled compound is a little more toxic than Isoniazid. Both titled compound and isoniazid show a positive AMES toxicity test implying that they may act as carcinogens. The maximum recommended tolerated dose (MRTD) provides an estimate of the toxic dose threshold of chemicals in humans. For a given compound, a MRTD of less than or equal to 0.477 log(mg/kg/day) is considered low, and high if greater than 0.477 log(mg/kg/day). The modeled structure (APTC) has a low MRTD and the Standard drug isoniazid has a high MRTD. The predicted lowest dose of a compound that results in an observed adverse effect is 0.764 for the titled compound and 2.824 for isoniazid. Both the studied compound and the standard drug are not associated with the normal functioning of the liver and also not associated with skin sensitization. Based on results from pharmacological data analysis, APTC has immense possibilities to be used as a standard drug for the treatment of tuberculosis (Tables 8a, 8b, 8c, 8d).

According to Fig. 5, the alkyl–π, π–π interaction and hydrogen bond stabilize the 1P45-ACDP complex (b). However, the 1P45-ACDP ligand–protein complex shows three hydrogen bond connections. At a distance of 2.470 and 2.963 Å, respectively, the ligand's atom N1 had branching hydrogen bond interactions with the atoms O_1 and O_2 of the active residues GLY14 and SER94. At a distance of 2.635 Å, the ligand's atom N2 forms bifurcated hydrogen bonds with the active residue GLY96's atom O3. Also seen in the ACDP-1P45 complex is one π–π interaction. At a distance of 3.983 Å, the six-membered ring of the residue PHE41 interacts with the benzene ring C1–C6 to form a hydrophobic bond. Further, four alkyl–*π* interactions are also observed in such a way that the CB-CG1 of the protein interacts with the benzene ring C1–C6 at a distance of 4.998 and 5.170, respectively constituting alkyl–*π* hydrophobic interactions, CB-CG1 of the protein interacts with the thiophene ring of the ligand at a distance of 5.425 Å, CB atom of the protein interacts with the benzene ring C1–C6 at a distance of 4.321 Å.

According to Fig. 5, the hydrogen bond, alkyl–π, π–π, and interaction bring the 4TZK-ACDP complex to steady state (c). In the 4TZK-ACDP complex, there is one hydrogen

Table 8 (a) Binding energy, hydrogen bond, and hydrophobic contacts of APTC with 1P44 protein

Inhibitor	Binding energy (kcal/mol)	Interactions	Distance	Bonding	Bonding types	Binding site of protein	Binding site of ligand
Ring	-8.00	ASP42[OD1.. H1-N1], ASP42[OD2.. H1-N1], PHE41[π..π]	2.579, 2.489, 3.905	Hydrogen, Hydrogen, Hydrophobic	H-bond, H-bond, π...π	OD1, OD2, Six membered ring	N1, N1, C1–C6 Benzene
Ring		ILE16[Alkyl… π]	5.133	Hydrophobic	Alkyl–π	CB-CG1	Thiophene
APTC ring		ILE16[Alkyl…π]	5.039	Hydrophobic	Alkyl–π	CB-CG1	C1–C6 Benzene
C6 Ring		VAL65[Alkyl…π]	4.627	Hydrophobic	Alkyl–π	CB-CG1	C1-Benzene
C6 Ring		ILE95[Alkyl…π]	4.627	Hydrophobic	Alkyl–π	CB-CG1	C1-Benzne
C6 Ring		ILE122[Alkyl…π]	5.020	Hydrophobic	Alkyl–π	CB-CG1	C1-Benzne

Table 8 (b) Binding energy, hydrogen bond, and hydrophobic contacts of APTC with 1P45 protein

Inhibitor,	Binding energy (kcal/mol)	Interactions	Distance	Bonding	Bonding types	Binding site of protein	Binding site of ligand
Ring	− 8.40	GLY14[OD1.. H1-N1], SER94[OD2.. H1-N1], GLY96[π..π]	2.470, 2.963, 2.635	Hydrogen, Hydrogen, Hydrogen	H-bond, H-bond, H-bond	O1, O2, O3	N1, N1, N2
Ring		PHE41[π…π]	3.983	Hydrophobic	π–π	Six membered ring	C1–C6 Benzene
APTC ring		ILE16[Alkyl…π]	5.425	Hydrophobic	Alkyl–π	CB-CG1	C1–C6
C6 Ring		ILE16[Alkyl…π]	4.998	Hydrophobic	Alkyl–π	CB-CG1	C1-Benzene
C6 Ring		ALA198[Alkyl…π]	4.321	Hydrophobic	Alkyl–π	CB	C1-Benzne
C6 Ring		ILE95[Alkyl…π]	5.1750	Hydrophobic	Alkyl–π	CB-CG1	C1–C6 Benzene

Table 8 (c) Binding energy, hydrogen bond, and hydrophobic contacts of APTC with 3FNE protein

Inhibitor	Binding energy (kcal/mol)	Interactions	Distance	bonding	Bonding types	Binding site of protein	Binding site of ligand
Ring	− 8.20	SER94[OD1.. H1-N1], PHE41[π..π]	2.490, 3.734	Hydrogen, Hydrophobic	H-bond,	Six membered ring	N1, C1–C6 Benzene
Ring		PHE41[π…π]	4.961	Hydrophobic	π–π	Six membered ring	C1–C6 Benzene
APTC ring		ILE16[Alkyl…π]	5.241	Hydrophobic	Alkyl–π	CB-CG1	Thiophene
C6 Ring		ILE16[Alkyl…π]	4.8784	Hydrophobic	Alkyl–π	CB-CG1	C1–C6 Benzene
C6 Ring		VAL65[Alkyl…π]	4.321	Hydrophobic	Alkyl–π	CB	C–Benzene
C6 Ring		ILE95[Alkyl…π]	5.208	Hydrophobic	Alkyl–π	CB-CG1	C1–C6 Benzene
C6 Ring		ILE95[Alkyl…π]	5.397	Hydrophobic	Alkyl–π	CB-CG1	Thiophene

Table 8 (d) Binding energy, hydrogen bond, and hydrophobic contacts of APTC with 4TZK protein

Inhibitor	Binding energy (kcal/mol)	Interactions	Distance	bonding	Bonding types	Binding site of protein	Binding site of ligand
Ring	− 8.30	PHE41[π…π], GLY14[O1…H1-N1]	2.941, 3.724	Hydrogen, Hydrophobic	H-bond, π...π	O1 Six membered ring	N1, C1–C6 Benzene
Ring		PHE41[π…π]	5.000	Hydrophobic	π…π	Six membered ring	Thiophene
APTC ring		ILE16[Alkyl…π]	4.759	Hydrophobic	Alkyl–π	CB-CG1	C1–C6 Benzene
C6 Ring		ILE16[Alkyl…π]	5.233	Hydrophobic	Alkyl–π	CB-CG1	C1–C6 Benzene
C6 Ring		VAL65[Alkyl…π]	5.292	Hydrophobic	Alkyl–π	CB-CG1	C1–C6 Benzene
C6 Ring		ILE122[Alkyl…π]	5.208	Hydrophobic	Alkyl–π	CB-CG1	C1–C6 Benzene

bond interaction that is seen. At a distance of 2.490 Å, the atom N1 of ACDP forms branching hydrogen bonds with the atom O1 of the active residue SER94. Furthermore, there are two π–π interactions found in the ACDP-4TZK complex. At distances of 3.734 and 4.961 Å, respectively, the six-membered ring of the residue PHE41 joins with the benzene ring C1–C6 of the ligand to form—hydrophobic interactions. Furthermore, five alkyl–π interactions are also discovered in such a way that the CB-CG1 of the protein PHE41 reacts with the benzene ring C1–C6 at a distance of 4.874 and 5.208 Å, respectively generating alkyl–π hydrophobic interactions, CB-CG1 of the protein ILE16 and ILE95 interacts with the thiophene ring of the ligand at a distance of 5.241 and 5.357 Å, respectively, CB-CG1 of the protein ILE16 and ILE95 interacts with the benzene ring C1–C6 of the ligand at a distance of 4.874 and 5.208 Å, respectively, CB atom of the protein VAL65 interacts with the benzene ring C1–C6 at a distance of 5.035 Å.

The 3FNE-ACDP complex is balanced by hydrogen bond and alkyl–π, π–π interaction as depicted in Fig. 5d. As observed, one hydrogen bond interaction is revealed in the 3FNE-ACDP complex. In like manner, the atom N1 of ACDP has bifurcated hydrogen bond interactions with the atom O1 of the active residue GLY14 at a distance of 2.941 Å. Also, two π–π interactions are observed in the ACDP-3FNE complex. The six-membered ring of the residue PHE41 interacts with the benzene ring C1–C6 of the ligand forming π–π hydrophobic interactions at a distance of 3.724 and 5.000 Å, respectively. Moreover, five alkyl–π interactions are also noticed in such a way that the CB-CG1 of the protein ILE16 combines with the benzene ring C1–C6 at a distance of 5.233 Å creating alkyl–π hydrophobic interaction, CB-CG1 of the protein ILE16 reacts with the thiophene ring of the ligand at a distance of 4.759 Å, CG1 of the protein VAL65 and ILE122 interacts with the benzene ring C1–C6 of the ligand at a distance of 5.292 and 5.208 Å, respectively.

The significant part of the docking studies is that three hydrogen bond interactions were observed in the

Table 9 (a) Docking of GEQ with selected inhA proteins

Proteins	Binding energy	Hydrogen bonds	RMSD
1P44	− 10.9	2	0.3
1P45	− 7.9	2	2
3FNE	− 7.9	1	3.6

Table 9 (b) Docking of D11 with selected inhA proteins

Proteins	Binding energy	Hydrogen bonds	RMSD
1P44	− 7.3	2	1.1
1P45	− 7.2	2	2.9
3FNE	− 7.4	2.3	2

Table 9 (c) Docking of 8PCwith selected inhA proteins

Proteins	Binding Energy	Hydrogen Bonds	RMSD
1P44	− 5.4	2	1.6
1P45	− 6.0	2	1.1
3FNE	− 6.6	2	0.5

Table 9 (d) Docking of 8PS with selected inhA proteins

Proteins	Binding energy	Hydrogen bonds	RMSD
1P44	− 3.8	2	2.4
1P45	− 5.2	2	2.9
3FNE	− 7.1	3	2.1

Table 9 (e) Docking of AYM with selected inhA proteins

Proteins	Binding energy	Hydrogen bonds	RMSD
1P44	− 6.9	1	2.7
1P45	− 7.7	2	1.0
3FNE	− 6.9	1	2.4

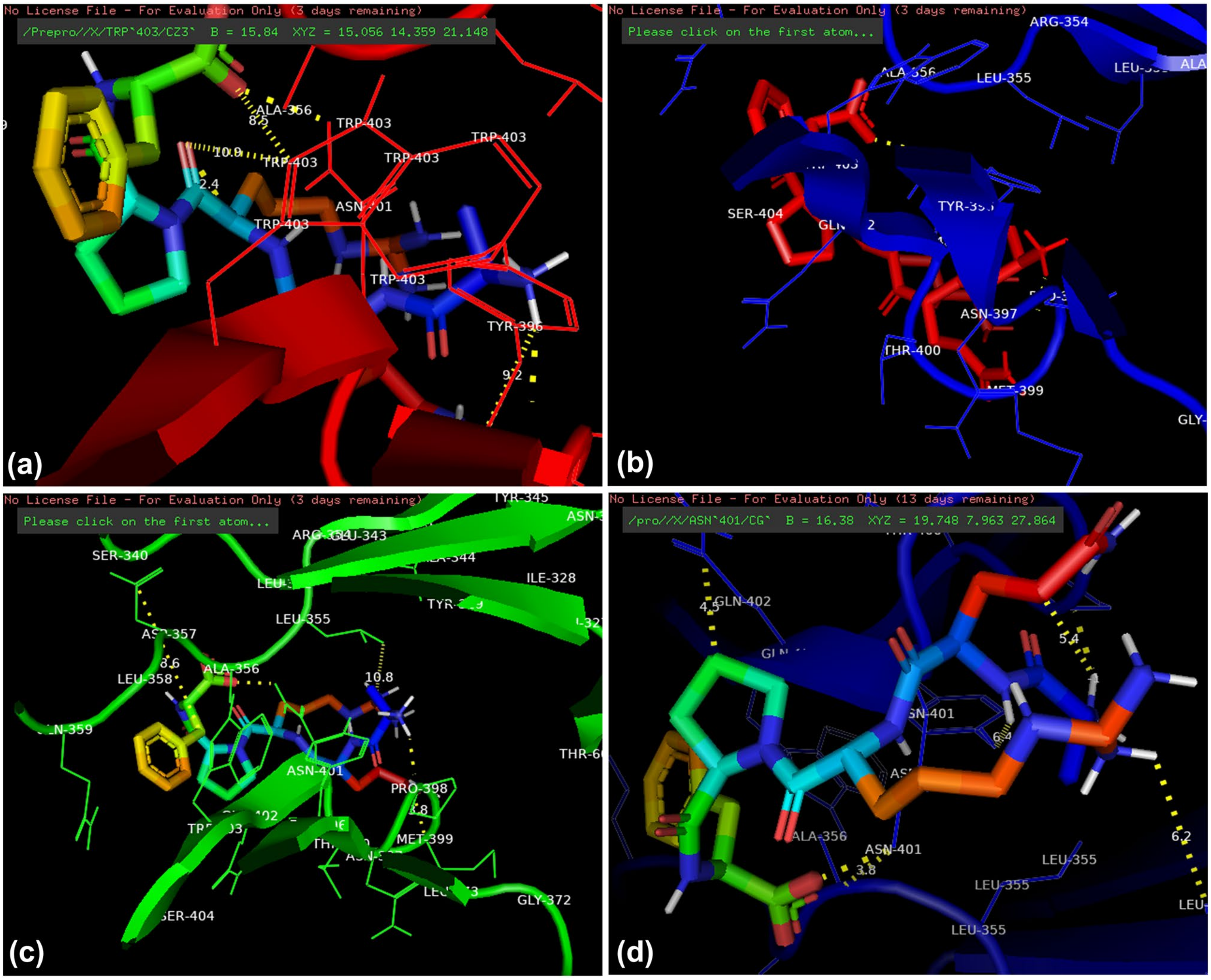

Fig. 5 **a** Interaction of studied compound to 1P44 binding site and Binding mode of studied compound at the binding site of 1P44. **b** Interaction of studied compound to 1P45 binding site and Binding mode of studied compound at the binding site of 1P45. **c** Interaction of studied compound to 3FNE binding site and Binding mode of studied compound at the binding site of 3FNE. **d** Interaction of studied compound to 4TZK binding site and Binding mode of studied compound at the binding site of 4TZK

1P45-ACDP complex. However, the ligand–protein interactions of 1P45-GEQ, 1P45-d11, 1P45-8PC, 1P45-8PS, and 1P45-AYM complexes which are originally used as Ligands for the selected InhA proteins yielded interactions with hydrogen bonds less than or equal to two [63] as shown in Tables 9a, 9b, 9c, 9d, 9e. Moreover, the docked 1P45-ACDP complex has a higher binding energy − 8.40 than all the other protein–ligand complexes except the 1P45-GEQ complex with binding energy − 9.20 which may be due to a greater number of hydrophobic interactions when compared to 1P45-ACDP complex. 1P44 has two hydrogen interactions when compared to already studied complexes only 1P45-GEQ has 2 hydrogen bond interactions, others (1P44-d11, 1P44-8PC, 1P44-8PS, and 1P44-AYM complexes) do not form hydrogen bonds with 1P44. The binding energy of the 1P44-ACDP complex is − 8.00, which is higher than all other protein–ligand complexes except 1P45-GEQ 10.9 which may also be due to higher hydrophobic interactions. 4TZK and 3FNE give one hydrogen interaction and a good number of hydrophobic interactions with a binding energy of − 8.20 and − 8.30, respectively. The existence of hydrogen and hydrophobic interactions identifies the increase in binding affinity and bioactivity of APTC when compared to other ligands.

These results recommend that the compound might be suitable as an inhibitor for inhA Proteins present in *Mycobacterium tuberculosis*. Hence, the studied compound may be regarded as a suitable drug for producing more tuberculosis drugs.

4 Conclusion

This research studies were focused on the experimental, DFT, and molecular docking studies of azo dyes synthesized by the reaction of diazotised 4-Aminobenzene-4-β-Sulphatoethylsulphone and 2-amino-4-(4-aminophenyl) thiophene-3-carbonitrile (AATC). The experimentally synthesized azo dye compound was characterized by FT-IR and GC–MS spectroscopy. The experimental measured FT-IR was reported in comparison with the theoretical vibrational DFT calculation. PED of normal modes of vibrations was done using the Veda 04 program. MESP and Local descriptors predict the most reactive part of the reduced modelled azo dye compound (ACDP). MESP and Condensed Dual Descriptor (Local Descriptors) predicted almost the same sites of the molecule as the most reactive in the compound. Excitation energy analysis predicted the types of electron excitations inherent in the five excited states of the compound. The lower band gap of the compound indicates the presence of a nonlinear optical (NLO) effect and this confirms the biological activity of the compound. Aromaticity indices (PDI, FLU, FLU-π, PLR, HOMA, BIRD) predicts the most stable and less stable aromatic ring fragment of the compound and their predictions correspond. The studied compound was found to display good NLO properties as the first hyperpolarizability is 93 times greater than that of Urea. Hence, it can serve as a suitable material for various technological applications. The Molecular docking results suggest that the compound might exhibit inhibitory action against InhA proteins which are responsible for *Mycobacterium tuberculosis* hence applied as an anti-tuberculosis agent. The ADMET results also suggest that the compound can be used as a drug as it obeys Lipinski RO5 and also yielded good results in comparison with Isoniazid. Therefore, we hope that the results help researchers in synthesizing other novel Anti-tubercular drugs.

Supplementary Information The online version contains supplementary material available at https://doi.org/10.1007/s42250-022-00544-9.

Acknowledgements The authors are thankful to Dr. J.E. Ishegbe of the Department of Polymer and Textile Engineering, Ahmadu Bello University for the method of synthesis, characterization, and spectroscopic analysis.

Funding This research work was not funded by any external funding agencies.

Availability of Data and Materials Not applicable.

Declarations

Conflict of interest The authors declare in unity zero conflict of interest.

References

1. Hashemi SH, Kaykhaii M (2022) Azo dyes: sources, occurrence, toxicity, sampling, analysis, and their removal methods. Emerging freshwater pollutants. Elsevier, Amsterdam, pp 267–287
2. Gürses A, Açıkyıldız M, Günes K, Gürses MS (2016) Classification of dye and pigments. Dyes and pigments. Springer, New York, pp 31–45
3. Yao LW, Khan FSA, Mubarak NM, Karri RR, Khalid M, Walvekar R et al (2022) Insight into immobilization efficiency of Lipase enzyme as a biocatalyst on the graphene oxide for adsorption of Azo dyes from industrial wastewater effluent. J Mol Liq 354:118849
4. Selvaraj V, Karthika TS, Mansiya C, Alagar M (2021) An over review on recently developed techniques, mechanisms and intermediate involved in the advanced azo dye degradation for industrial applications. J Mol Struct 1224:129195
5. Kapoor RT, Danish M, Singh RS, Rafatullah M, Hps AK (2021) Exploiting microbial biomass in treating azo dyes contaminated wastewater: mechanism of degradation and factors affecting microbial efficiency. J Water Process Eng 43:102255
6. Dulo B, Phan K, Githaiga J, Raes K, De Meester S (2021) Natural quinone dyes: A review on structure, extraction techniques, analysis and application potential. Waste Biomass Valorization 12(12):6339–6374
7. Shankarling GS, Deshmukh PP, Joglekar AR (2017) Process intensification in azo dyes. J Environ Chem Eng 5(4):3302–3308
8. Pedgaonkar GS, Sridevi JP, Jeankumar VU, Saxena S, Devi PB, Renuka J, Sriram D (2014) Development of 2-(4-oxoquinazolin-3(4H)-yl) acetamide derivatives as novel enoyl-acyl carrier protein reductase (InhA) inhibitors for the treatment of tuberculosis. Eur J Med Chem 86:613–627
9. Freundlich JS, Wang F, Vilchèze C, Gulten G, Langley R, Schiehser GA et al (2009) Triclosan derivatives: towards potent inhibitors of drug-sensitive and drug-resistant *Mycobacterium tuberculosis*. ChemMedChem 4(2):241
10. Romano E, Castillo MV, Pergomet JL, Zinczuk J, Brandán SA (2012) Synthesis and structural and vibrational analysis of (5, 7-dichloro-quinolin-8-yloxy) acetic acid. J Mol Struct 1018:149–155
11. Frisch MJ (2009) Gaussian09. http://www.gaussian.com/
12. Xu X, Goddard WA (2004) The X3LYP extended density functional for accurate descriptions of nonbond interactions, spin states, and thermochemical properties. Proc Natl Acad Sci 101(9):2673–2677
13. Karabulut E (2018) Linear reaction of Ca atom with HCl molecule in the ground electronic state: Hartree-Fock method. J Phys Chem Funct Mater 1(2):43–48
14. Jamroz MH (2004) Vibrational energy distribution analysis VEDA 4
15. Lu T, Chen F (2012) Multiwfn: a multifunctional wavefunction analyzer. J Comput Chem 33(5):580–592
16. Robbins D, Newton AF, Gignoux C, Legeay JC, Sinclair A, Rejzek M et al (2011) Synthesis of natural-product-like scaffolds in unprecedented efficiency via a 12-fold branching pathway. Chem Sci 2(11):2232–2235
17. Murugavel S, Kannan D, Bakthadoss M (2017) Synthesis of a novel methyl (2E)-2-{[N-(2-formylphenyl)(4-methylbenzene) sulfonamido] methyl}-3-(2-methoxyphenyl) prop-2-enoate: Molecular structure, spectral, antimicrobial, molecular docking and DFT computational approaches. J Mol Struct 1127:457–475
18. Pires DE, Blundell TL, Ascher DB (2015) pkCSM: predicting small-molecule pharmacokinetic and toxicity properties using graph-based signatures. J Med Chem 58(9):4066–4072

19. Trott O, Olson AJ (2010) AutoDock Vina: improving the speed and accuracy of docking with a new scoring function, efficient optimization, and multithreading. J Comput Chem 31(2):455–461
20. Hanwell MD, Curtis DE, Lonie DC, Vandermeersch T, Zurek E, Hutchison GR (2012) Avogadro: an advanced semantic chemical editor, visualization, and analysis platform. J Cheminform 4(1):1–17
21. Guex N, Peitsch MC (1997) SWISS-MODEL and the Swiss-Pdb Viewer: an environment for comparative protein modeling. Electrophoresis 18(15):2714–2723
22. Gruswitz F, Chaudhary S, Ho JD, Schlessinger A, Pezeshki B, Ho CM et al (2010) Function of human Rh based on structure of RhCG at 2.1 Å. Proc Natl Acad Sci 107(21):9638–9643
23. Fakih TM, Dewi ML (2020) In silico identification of characteristics spike glycoprotein of SARS-CoV-2 in the development novel candidates for COVID-19 infectious diseases. J Biomed Transl Res 6(2):48–52
24. Shepard RA (2021) A Computational investigation of cathode materials for next-generation secondary batteries (Doctoral dissertation, State University of New York at Binghamton)
25. Abul-Futouh H, Abaalkhail SJ, Harb MK, Görls H, Weigand W (2021) Structural studies and electrochemical catalysis investigation of [FeFe]-hydrogenase H-cluster mimics mediated by monophosphane ligands. Polyhedron 207:115382
26. Siebert S, Döll P (2010) Quantifying blue and green virtual water contents in global crop production as well as potential production losses without irrigation. J Hydrol 384(3–4):198–217
27. Krishnakumar V, Jayamani N, Mathammal R, Parasuraman K (2009) Density functional theory calculations and vibrational spectra of 2-bromo-4-chloro phenol and 2-chloro-4-nitro phenol. J Raman Spectrosc 40(11):1551–1556
28. Singho ND, Lah NAC, Johan MR, Ahmad R (2012) FTIR studies on silver-poly (methylmethacrylate) nanocomposites via in-situ polymerization technique. Int J Electrochem Sci 7(6):5596–5603
29. Vennila P, Govindaraju M, Venkatesh G, Kamal C (2016) Molecular structure, vibrational spectral assignments (FT-IR and FT-RAMAN), NMR, NBO, HOMO-LUMO and NLO properties of O-methoxybenzaldehyde based on DFT calculations. J Mol Struct 1111:151–156
30. Bansal A, Singh R, Singh RV (2000) Toxicity, spectroscopic characterization and electrochemical behaviour of new macroclic complexes of lead (II) and palladium (II) metals. Met-Based Drugs 7(4):211–218
31. Wang JC, Wang PY, Huang RR, Lin WC, Fang CH, Pai LM, Nee TE (2011) Lie group study of Raman spectra of the Gurken gradient in Drosophila oogenesis. Anal Bioanal Chem 400(2):335–341
32. Rajesh AMMVP, Prabakaran AR, Gunasekaran S (2019) Extraction, Spectroscopic study of molecular structure and density functional theory studies Cis-vaccenic Acid from the leaves of Boswellia Serrata
33. Schwenke DW, Truhlar DG (1985) Systematic study of basis set superposition errors in the calculated interaction energy of two HF molecules. J Chem Phys 82(5):2418–2426
34. Gutowski M, van Duijneveldt-van de Rijdt JG, van Lenthe JH, van Duijneveldt FB (1993) Accuracy of the Boys and Bernardi function counterpoise method. J Chem Phys 98(6):4728–4737
35. Agwupuye JA, Louis H, Unimuke TO, David P, Ubana EI, Moshood YL (2021) Electronic structure investigation of the stability, reactivity, NBO analysis, thermodynamics, and the nature of the interactions in methyl-substituted imidazolium-based ionic liquids. J Mol Liq 337:116458
36. de Carvalho Marques Dourado JM (2021). Development and study of aminocatalyzed asymmetric organic reactions
37. Robb KA (2019) Enantioselective, Lewis base-catalyzed transformations: I. Polyene sulfenocyclization (preparative and mechanistic aspects) II. Sulfenofunctionalization of alkenyl boronates enabled by 1, 2-boronate migration (Doctoral dissertation, University of Illinois at Urbana-Champaign).
38. Karni O, Barré E, Pareek V, Georgaras JD, Man MK, Sahoo C et al (2022) Structure of the moiré exciton captured by imaging its electron and hole. Nature 603(7900):247–252
39. Yu C, Saalmann U, Rost JM (2022) High-order harmonics from backscattering of delocalized electrons. Phys Rev A 105(4):L041101
40. Mukherjee A, Lal S (2022) Superconductivity from repulsion in the doped 2D electronic Hubbard model: an entanglement perspective. J Phys: Condens Matter 34(27):275601
41. Solomatina AI, Kuznetsov KM, Gurzhiy VV, Pavlovskiy VV, Porsev VV, Evarestov RA, Tunik SP (2020) Luminescent organic dyes containing a phenanthro [9, 10-D] imidazole core and [Ir (N^ C)(N^ N)]+ complexes based on the cyclometalating and diimine ligands of this type. Dalton Trans 49(20):6751–6763
42. Kraner S, Prampolini G, Cuniberti G (2017) Exciton binding energy in molecular triads. J Phys Chem C 121(32):17088–17095
43. Pearson RG (1988) Electronic spectra and chemical reactivity. J Am Chem Soc 110(7):2092–2097
44. Benjamin I, Udoikono AD, Louis H, Agwamba EC, Unimuke TO, Owen AE, Adeyinka AS (2022) Antimalarial potential of naphthalene-sulfonic acid derivatives: Molecular electronic properties, vibrational assignments, and in-silico molecular docking studies. J Mol Struct 1264:133298
45. Agwamba EC, Udoikono AD, Louis H, Udoh EU, Benjamin I, Igbalagh AT et al (2022) Synthesis, characterization, DFT studies, and molecular modeling of azo dye derivatives as potential candidate for trypanosomiasis treatment. Chem Phys Impact 4:100076
46. Eno EA, Mbonu JI, Louis H, Patrick-Inezi FS, Gber TE, Unimke TO et al (2022) Antimicrobial activities of 1-phenyl-3-methyl-4-trichloroacetyl-pyrazolone: Experimental, DFT studies, and molecular docking investigation. J Indian Chem Soc 99:100524
47. Edet HO, Louis H, Benjamin I, Gideon M, Unimuke TO, Adalikwu SA, Nwagu AD, Adeyinka AS (2022) Hydrogen storage capacity of C12X12 (X= N, P, and Si). Chem Phys Impact 5:100107
48. Inah BE, Hitler L, Innocent B, Unimuke T, Adeyinka AS (2022) Computational study on the interactions of functionalized C24NC (NC= C-OH,-NH2,–COOH, and B) with chloroethylphenylbutanoic acid. Can J Chem. https://doi.org/10.1139/cjc-2022-0181
49. Gber TE, Louis H, Owen AE, Etinwa BE, Benjamin I, Asogwa FC et al (2022) Heteroatoms (Si, B, N, and P) doped 2D monolayer MoS 2 for NH 3 gas detection. RSC Adv 12(40):25992–26010
50. Louis H, Charlie DE, Amodu IO, Benjamin I, Gber TE, Agwamba EC, Adeyinka AS (2022) Probing the reactions of thiourea (CH4N2S) with Metals (X= Au, Hf, Hg, Ir, Os, W, Pt, and Re) Anchored on Fullerene Surfaces (C59X). ACS Omega 7:35118–35135
51. Makhlouf J, Louis H, Benjamin I, Ukwenya E, Valkonen A, Smirani W (2022) Single crystal investigations, spectral analysis, DFT studies, antioxidants, and molecular docking investigations of novel hexaisothiocyanato chromate complex. J Mol Struct 134223
52. Pedersen J, Mikkelsen KV (2022) A benchmark study of aromaticity indexes for benzene, pyridine and the diazines–I. Ground state aromaticity. RSC Adv 12(5):2830–2842
53. Manassir M, Pakiari AH (2022) Valence non-Lewis density as an approach to describe and measure aromaticity of organic and inorganic molecules. J Mol Graph Model 110:108062
54. Matito E, Salvador P, Duran M, Solà M (2006) Aromaticity measures from Fuzzy-Atom Bond Orders (FBO). The Aromatic

fluctuation (FLU) and the para-delocalization (PDI) indexes. J Phys Chem A 110(15):5108–5113
55. Apebende CG, Idante PS, Louis H, Ameuru US, Unimuke TO, Gber TE et al (2022) Integrated spectroscopic, bio-active prediction and analytics of isoquinoline derivative for breast cancer mitigation. Chem Africa. https://doi.org/10.1007/s42250-022-00479-1
56. Agwamba EC, Louis H, Benjamin I, Apebende CG, Unimuke TO, Edet HO et al (2022) (E)-2-((3-nitrophenyl) diazenyl)-3-oxo-3-phenylpropanal: experimental, DFT studies, and molecular docking investigations. Chem Africa. https://doi.org/10.1007/s42250-022-00468-4
57. Benjamin I, Gber TE, Louis H, Ntui TN, Oyo-Ita EI, Unimuke TO et al (2022) Modelling of aminothiophene-carbonitrile derivatives as potential drug candidates for hepatitis B and C. Iran J Sci Technol Trans A Sci. https://doi.org/10.1007/s40995-022-01355-w
58. Clavian LM, Kumar KA, Rao DN, Shihab NK, Sanjeev G, Kumar PR (2022) Influence of structural and morphological features of zinc (II)-tetraphenylporphyrin thin film on its third order optical nonlinearity at pico and nano second regimes. J Lumin 246:118835
59. Qian J, Feng Z, Fan X, Kuzmin A, Gomes AS, Prasad PN (2022) High contrast 3-D optical bioimaging using molecular and nanoprobes optically responsive to IR light. Phys Rep 962:1–107
60. Semin S, Li X, Duan Y, Rasing T (2021) Nonlinear optical properties and applications of fluorenone molecular materials. Adv Opt Mater 9(23):2100327
61. Mohanraj P, Sivakumar R, Massoud EES (2022) Role of higher order dispersion on instability criterion of saturable fiber system with non-Kerr nonlinearities. Optik 253:168608
62. Al-Sulami AI, Basha MT, Althagafy HS, Al-Zaydi KM, Davaasuren B, Al-kaff NS, Said MA (2022) Azo-based multifunctional molecules and their copper (II) complexes as potential inhibitors against Alzheimer's disease: XRD/Hirshfeld analysis/DFT/molecular docking/cytotoxicity. Inorg Chem Commun 142:109535
63. Stigliani JL, Bernardes-Génisson V, Bernadou J, Pratviel G (2012) Cross-docking study on InhA inhibitors: a combination of Autodock Vina and PM6-DH2 simulations to retrieve bio-active conformations. Org Biomol Chem 10(31):6341–6349